Parameterized Digital Finite Element Analysis of Hybrid Steel-BFRP Reinforced Concrete Beams Using ANSYS Workbench

Ravshanbek Mavlonov[1], Kamoliddin Muminov[1], Abdurasul Martazaev[1], Sokhiba Numanova[2], Odiljon Fozilov[1] and Venkatesh Kodur[3]

[1]*Department of Construction of Buildings and Structures, Namangan State Technical University, Islam Karimov Ave. 12, 160720 Namangan, Uzbekistan*

[2]*Department of Civil Engineering, Namangan State Technical University, Islam Karimov Ave. 12, 160720 Namangan, Uzbekistan*

[3]*Department of Civil and Environmental Engineering, Michigan State University, 3574 Engineering Building, 428 S. Shaw Lane, 48824 East Lansing, MI, USA*

ravshanbek.mavlonov@gmail.com, kamoliddin.komiljonovich.86@gmail.com, abdurasul.mas@gmail.com, sohibanomanova@gmail.com, odiljon690.21.03@gmail.com, kodur@egr.msu.edu

Keywords: Digital Finite Element Modeling, ANSYS Workbench, Parametric Simulation, Nonlinear Structural Analysis, Hybrid Steel-BFRP Reinforcement, Concrete Strain, Computational Engineering.

Abstract: This study develops a parameterized digital finite element workflow for comparative analysis of reinforced concrete beams with steel and hybrid steel-basalt fiber reinforced polymer (BFRP) reinforcement. Nine reinforcement configurations were represented within a common ANSYS Workbench environment using identical geometry, loading, boundary conditions, mesh strategy, and nonlinear concrete constitutive assumptions. Concrete nonlinearity was represented using a coupled damage-plasticity microplane formulation with a smooth three-surface Drucker-Prager cap yield function, whereas steel and BFRP reinforcement were represented through their respective elastic and strength parameters. The digital workflow enabled systematic extraction and comparison of tensile and compressive concrete strains, reinforcement stress development, tensile-damage initiation response, steel-yielding stages, and ultimate flexural behavior across three reinforcement series. The simulations showed that reinforcement composition substantially affects concrete strain development after cracking. Hybrid steel-BFRP beams exhibited earlier redistribution of internal forces and altered tensile-strain growth, while increased longitudinal reinforcement area reduced concrete deformation. The principal contribution is not a new constitutive law but a reproducible computational framework for comparing multiple reinforcement configurations under controlled numerical conditions. The proposed workflow demonstrates how nonlinear finite element simulation can support digital structural assessment and preliminary reinforcement-design decisions before extensive physical testing.

1 INTRODUCTION

Reinforced concrete beams remain fundamental structural members, but conventional steel reinforcement is vulnerable to corrosion in aggressive environments. Fiber-reinforced polymer (FRP) reinforcement offers high tensile strength and corrosion resistance, while its linear-elastic response up to rupture can reduce ductility. Hybrid steel-FRP systems combine the yielding and redistribution capacity of steel with the durability and tensile contribution of FRP, providing a practical balance between serviceability and ultimate performance [1]-[3].

Recent experimental and analytical work on hybrid steel-FRP beams has mainly examined flexural strength, deflection, cracking, and serviceability. A recent study by Mavlonov et al. [4] also combined analytical and experimental assessment of hybrid steel-FRP beams, reinforcing the need for comparable strain-level indicators across reinforcement configurations. Related investigations of concrete systems containing combined steel and basalt-based reinforcement have also shown that reinforcement composition measurably affects tensile response [5], further motivating strain-level numerical comparison when basalt-based reinforcement is incorporated into concrete members.

Digital numerical and computational analysis is increasingly used to extend laboratory investigations by creating repeatable model sets and extracting structural or material-response indicators that are difficult to monitor continuously in physical tests. Computational assessment has also been applied to the theoretical evaluation of concrete mechanical properties and variability [6]. ANSYS-based modeling of reinforced concrete structures [7] demonstrates the value of consistent digital model construction. Comparable computational structural-assessment approaches have used nonlinear pushover analysis to derive performance-relevant response indicators [8] and dynamic modeling based on measured earthquake records to evaluate engineering-system response under controlled numerical input [9]. Numerical-model-based soft-computing concepts [10] and finite element analysis of hybrid reinforcement systems [11] further illustrate the growing role of computational environments in structural assessment.

Finite element studies can represent nonlinear material response and provide configuration-specific stress and strain fields under controlled loading conditions. Combined experimental-numerical work has demonstrated the value of controlled simulation for hybrid steel-GFRP beams [12], while computational design studies have addressed flexural capacity and reinforcement selection [13], [14]. However, the numerical workflow itself is often treated as a secondary implementation detail rather than as a standardized comparative-analysis framework.

Concrete tensile and compressive strains are important indicators of crack development, serviceability, neutral-axis evolution, and compression-zone failure. Hybrid reinforcement changes post-cracking stiffness and load redistribution, making strain-compatible comparison particularly important when steel and FRP proportions vary [2]-[4].

Nevertheless, fewer studies describe how several steel-BFRP configurations can be organized within one parameterized digital environment using common geometry, loading, material data, mesh resolution, and output variables. Without such standardization, differences between independently prepared numerical models may be confounded with reinforcement effects.

This study addresses that computational gap by developing a common ANSYS Workbench finite element workflow for nine beam configurations grouped into three reinforcement series. The objective is to compare tensile and compressive concrete strain development under standardized numerical conditions and to demonstrate a reproducible digital workflow for configuration screening. The study does not propose a new constitutive law; its contribution is the controlled organization, execution, and interpretation of nonlinear finite element models as a comparative digital assessment system.

This study provides a common parameterized ANSYS Workbench modeling framework for nine steel and hybrid steel-BFRP beam configurations, enabling a standardized numerical representation of beam geometry, loading conditions, boundary constraints, mesh resolution, concrete nonlinearity, and reinforcement properties. The developed digital workflow allows the extraction and comparison of tensile and compressive concrete strains at consistent normalized loading stages. Furthermore, the proposed approach establishes a configuration-level assessment framework that links reinforcement composition with numerically obtained strain development and flexural response, supporting a systematic evaluation of different reinforcement strategies.

2 DIGITAL FINITE ELEMENT METHODOLOGY

Figure 1 illustrates the structural scheme of a single-span reinforced concrete beam with a rectangular cross-section. The total length of the beam was l=1500 mm, while the effective (calculated) span length was l_0=1400 mm. The cross-sectional dimensions were defined by a height h=200 mm and a width b=150 mm. In order to investigate the beam behavior with respect to normal sections, the applied concentrated load was positioned at a distance of $l_0/3$ from the support.

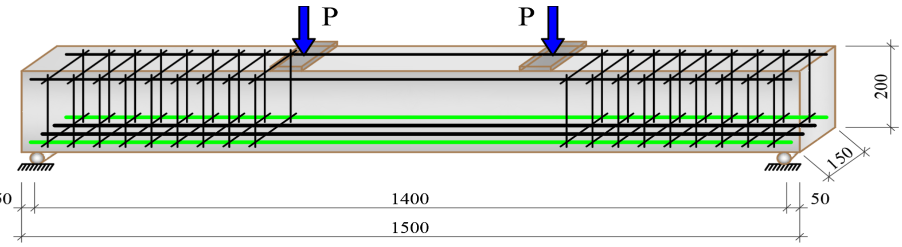

Figure 1: Beam geometry and reinforcement layout (B5-2S12-2F12).

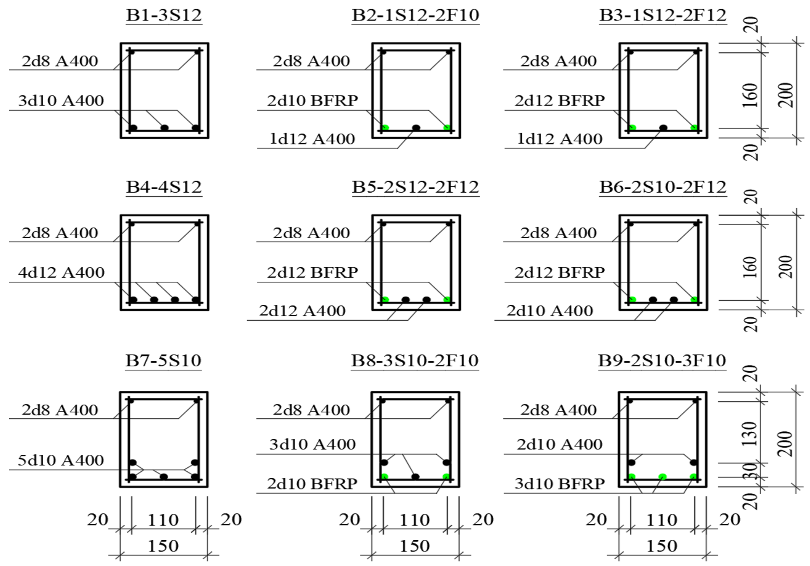

Figure 2: Cross sections of the beams.

Figure 2 shows the cross-sections of the samples. For the numerical analysis, three groups comprising nine reinforcement configurations were defined. Among them, six specimens (B2-1S12-2F10, B3-1S12-2F12, B5-2S12-2F12, B6-2S10-2F12, B8-3S10-2F10, and B9-2S10-3F10) were reinforced using a combination of steel and BFRP bars. The remaining three specimens (B1-3S12, B4-4S12, and B7-5S10) were reinforced exclusively with steel bars and were considered as control beams for comparison with the hybrid-reinforced specimens.

The nine beam configurations were treated as a controlled digital model set. Each configuration retained the same global beam geometry, loading scheme, support conditions, and finite element discretization, while the longitudinal reinforcement definition was modified according to the configuration code. This structure enabled direct cross-configuration comparison and reduced differences associated with independent model preparation.

In all beam specimens, transverse reinforcement was provided using d=6 mm A240 class steel stirrups. Considering that the numerical investigation focused on the behavior of the beams under bending with respect to normal sections, the spacing of transverse reinforcement was set to 50 mm within the support regions extending over *l*/4, while no transverse reinforcement was installed in the central region covering *l*/2 of the span, as shown in Figure 1. A reinforcement layout of this type was chosen with the purpose of making certain that failure would be by predominantly flexural rather than shear behavior. The exclusion of transverse reinforcement in the mid-span area enabled a better assessment of the impact of longitudinal hybrid steel-BFRP reinforcement on crack initiation, crack propagation, strain generation as well as ultimate flexural capacity.

Hybrid reinforcement was introduced to combine the yielding and ductility of steel with the high tensile strength, corrosion resistance, and low mass of BFRP bars. By varying the number, diameter, and arrangement of steel and BFRP longitudinal bars across the specimen groups, the digital model set enabled systematic assessment of how reinforcement composition influenced the concrete stress-strain state in the tensile and compressive zones.

Common loading and reinforcement-detailing rules were retained across the model set so that the numerical comparison focused on the longitudinal steel-BFRP composition. The identical support and loading scheme were selected to promote flexural response and to provide comparable boundary conditions for all configurations.

2.1 Parameterized Digital Modeling Workflow

The numerical investigation was organized as a repeatable five-stage digital workflow: (1) configuration definition; (2) geometry and reinforcement assignment; (3) nonlinear material-model assignment; (4) meshing, loading, and boundary-condition application; and (5) extraction of strain and stress outputs for comparative analysis. The same sequence was applied to all nine configurations.

Configuration identifiers encoded the number and diameter of steel and BFRP longitudinal bars. For digital comparison, each beam configuration was defined by four reinforcement parameters: the number and diameter of steel bars and the number and diameter of BFRP bars. These parameters formed the configuration descriptor used in the model identifiers; for example, 2S12-2F12 denotes two 12-mm steel bars and two 12-mm BFRP bars. The remaining geometry, material, mesh, support, and loading parameters were kept constant across the digital model set. Reinforcement composition was therefore treated as the principal model variable, whereas geometry, span, load location, support conditions, transverse reinforcement strategy, and mesh size were controlled. The resulting outputs were grouped into three reinforcement series and compared using concrete tensile strain, concrete compressive strain, reinforcement stress development, and ultimate-stage response.

The digital models were implemented in ANSYS Workbench for nonlinear static analysis. A uniform finite element mesh size of 25 mm was adopted for all nine configurations to preserve computational comparability. Three-dimensional solid elements represented the concrete domain, while reinforcement definitions were embedded within the common beam geometry. Identical loading and support conditions were applied to each configuration. This standardized architecture isolated reinforcement composition as the principal comparative variable and follows the broader use of ANSYS-based digital modeling for reinforced concrete systems [7].

Concrete nonlinearity was represented using the coupled damage-plasticity microplane formulation implemented in ANSYS [15]. The formulation employs a smooth three-surface Drucker-Prager cap yield function together with tension-compression damage evolution and nonlocal regularization. The constitutive and nonlocal parameters used in the numerical models are summarized in Table 1. The same parameter set was assigned to every beam configuration to maintain a consistent numerical basis for cross-configuration strain comparison.

Table 1: Coupled damage-plasticity microplane concrete parameters used in all digital beam models.

Property	Symbol	Value	Unit
Modulus of elasticity	E	28766	MPa
Poisson's ratio	μ	0.2	
Uniaxial compressive strength	f_{uc}	37.46	MPa
Biaxial compressive strength	f_{bc}	43.08	MPa
Uniaxial tensile strength	f_{ut}	2.75	MPa
Tensile cap hardening factor	R_t	1	-
Hardening parameter	D	30000	MPa^2
Compressive cap location	σ^c_v	-28.72	MPa
Compressive cap shape	R	2	-
Threshold for tensile damage	γ_{t0}	0	-
Threshold for compressive damage	γ_{c0}	2×10^{-5}	-
Tension damage parameter	β_t	3000	-
Compressive damage parameter	β_c	2000	-
Nonlocal interaction range parameter	c	1600	mm^2
Over nonlocal parameter	m	2.5	-

Table 2: BFRP reinforcement parameters assigned to the digital models.

Property	Value	Unit
Modulus of elasticity	50240	MPa
Poisson's ratio	0.22	-
Yield strength	-	-
Ultimate strength	980	MPa

Table 3: Steel reinforcement parameters assigned to the digital models.

Property	Value	Unit
Modulus of elasticity	200000	MPa
Poisson's ratio	0.3	-
Yield strength	400	MPa
Ultimate strength	600	MPa

The BFRP properties used in the numerical models are listed in Table 2, while the steel-reinforcement properties are summarized in Table 3. Steel reinforcement was modeled using the specified elastic modulus, yield strength, and ultimate strength;

BFRP was represented as a linear-elastic reinforcement material up to rupture. Perfect bond between concrete and reinforcement was assumed consistently for all configurations.

The standardized output set included load-stage response, reinforcement stress development, and tensile and compressive concrete strain fields. These outputs formed the digital dataset used to compare reinforcement configurations and to evaluate strain redistribution, serviceability-related behavior, and ultimate-stage response.

3 DIGITAL SIMULATION RESULTS AND COMPARATIVE ANALYSIS

The standardized ANSYS workflow generated a common set of numerical outputs for all nine beam configurations. Extracted variables included concrete tensile and compressive strains, reinforcement stress development, normalized load-stage response, and ultimate-state deformation patterns. Because identical geometry, mesh resolution, loading, and concrete constitutive parameters were used, differences between configurations could be interpreted primarily in relation to longitudinal steel-BFRP reinforcement composition.

Figures 3-5 show representative ANSYS contour outputs at the ultimate stage for the three-reinforcement series. The control and hybrid configurations were evaluated under identical numerical conditions, allowing the deformation and stress patterns to be compared within the common digital model set.

As the applied load increased, the numerical response progressed from tensile-zone damage initiation to increasing reinforcement stress and accelerated beam deformation. At higher load levels, steel stresses approached the yield limit, followed by pronounced nonlinear deformation. The ultimate stage was characterized by compression-zone damage and a reduction in the numerical load-carrying response.

The numerical models reproduced a consistent flexural-response sequence from tensile-zone damage initiation through reinforcement stress development to accelerated deformation and ultimate compression-zone damage. This consistency supports comparative interpretation within the common model set; however, the study does not constitute independent experimental validation of the constitutive formulation.

The strain outputs were organized by reinforcement series to support configuration-level digital comparison. Rather than interpreting isolated contour plots, tensile and compressive concrete strains were compared as functions of the normalized load level M/Mu. This common load-stage representation enabled different configurations to be evaluated within one computational framework and made reinforcement-related changes in strain development easier to identify.

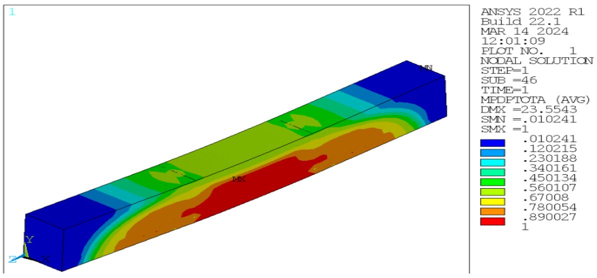

Figure 3: Representative ANSYS contour output for beam B3-1S12-2F12 at the ultimate load stage (Series 1).

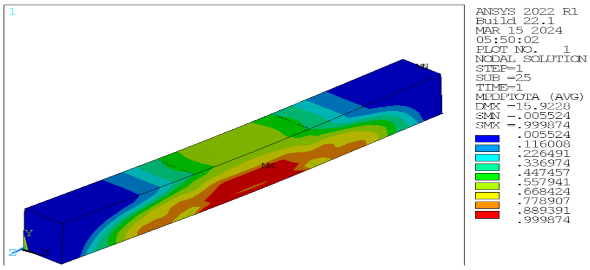

Figure 4: Representative ANSYS contour output for beam B5-2S12-2F12 at the ultimate load stage (Series 2).

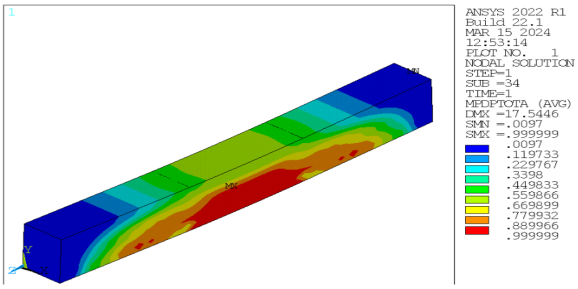

Figure 5: Representative ANSYS contour output for beam B9-2S10-3F10 at the ultimate load stage (Series 3).

Figure 6 illustrates the variation of concrete strains in the tensile and compressive zones of the Series 1 beams subjected to bending moments. As the applied load was gradually increased, the numerical tensile-zone damage initiation, corresponding to the onset of flexural cracking, occurred in all beams at approximately *(0.2…0.25)*M_u. Up to this loading stage, the relative concrete strains in both the conventional steel-reinforced concrete beams and the hybrid steel-BFRP beams increased at nearly identical rates, indicating similar elastic behavior.

With further loading, in beams reinforced solely with steel bars, the stress in the steel reinforcement reached its yield limit at load levels of $(0.85…0.89)M_u$. Beyond this point and until failure, the concrete strains in the compressive zone increased from $3.7×10^{-4}$ to $7.3×10^{-4}$, while the tensile concrete strains rose from $10.6×10^{-4}$ to $15.2×10^{-4}$. This behavior reflects an increase in beam ductility and the development of plastic deformations prior to failure.

In contrast, for beams reinforced with hybrid steel-BFRP reinforcement, yielding of the steel bars was observed at a comparatively earlier loading stage, namely at (0.7…0.75) M_u. The BFRP reinforcement, characterized by a lower elastic modulus than steel and a predominantly linear-elastic response up to rupture, altered the stiffness distribution and internal force sharing within the hybrid section. This change influenced stress redistribution between the concrete, steel, and BFRP reinforcement and consequently affected the overall deformation behavior of the beams.

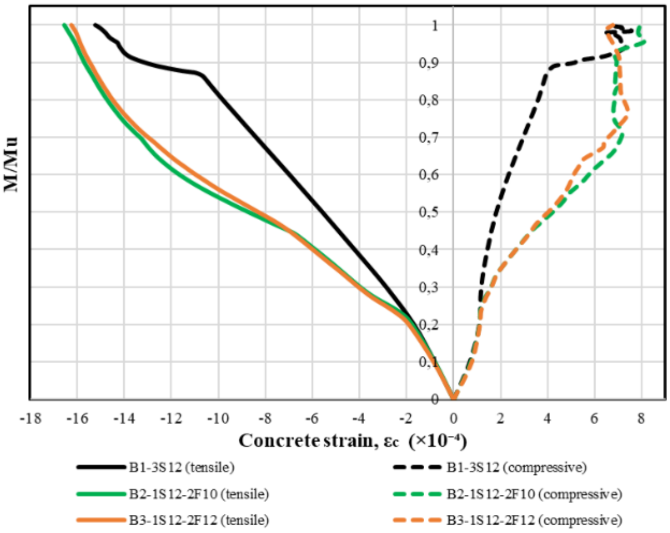

Figure 6: Normalized load-concrete strain response for Series 1.

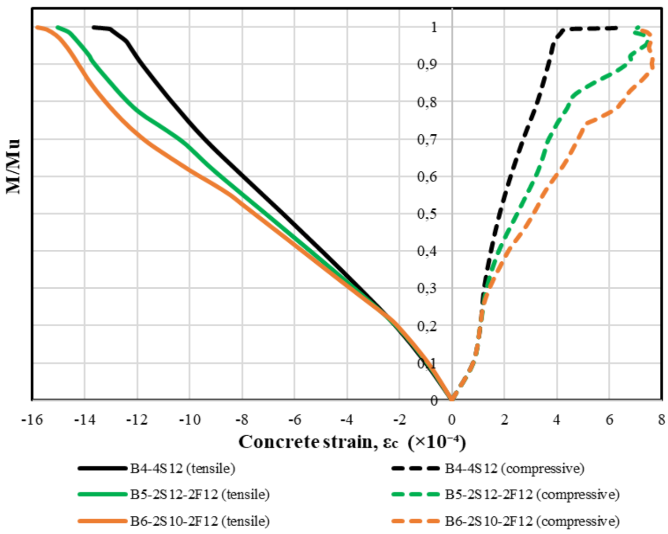

Figure 7: Normalized load-concrete strain response for Series 2.

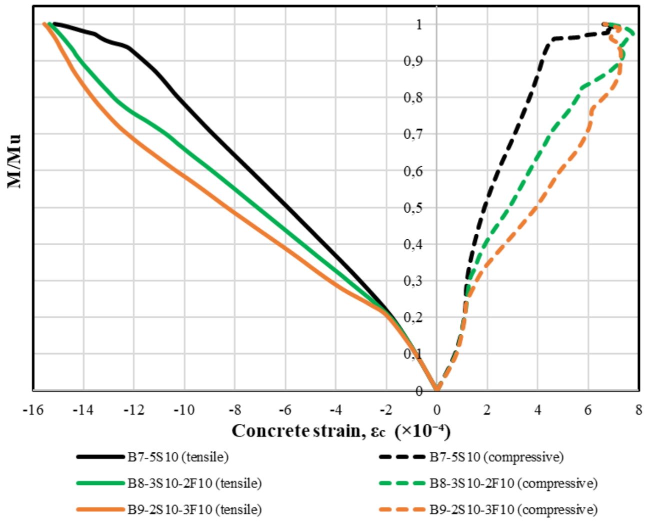

Figure 8: Normalized load-concrete strain response for Series 3.

The analysis further revealed that the ratio between concrete strains in the tensile and compressive zones ranged from 2.1 to 2.9, which is consistent with the typical deformation mechanism of reinforced concrete members subjected to flexural loading. The more uniform strain distribution obtained for the hybrid-reinforced beams indicates a different serviceability-related response within the common numerical model set; direct confirmation of stiffness improvement would require experimental validation.

Figure 7 shows compressive and tensile strains of the Series 2 specimens. The concrete strains in both the tensile and compressive zones exhibited nearly identical growth trends in beams reinforced solely with steel and in those reinforced with hybrid steel-BFRP bars during the initial loading stage, corresponding to $(0.2\ldots0.25)M_u$. This behavior indicates that all beams predominantly remained in the elastic range during the early phase of loading.

With increasing load levels, the evolution of concrete strains was found to be strongly influenced by the reinforcement ratio and the total cross-sectional area of the longitudinal reinforcement. In particular, the B6-2S10-2F12 beam, which had the smallest longitudinal reinforcement cross-sectional area, exhibited the largest concrete strain values. In contrast, the concrete strains observed in specimen B5-2S12-2F12 were intermediate, lying between those recorded for specimens B4-4S12 (reinforced only with steel) and B6-2S10-2F12. This trend clearly demonstrates that an increase in the reinforcement ratio leads to a reduction in concrete deformation under bending.

Beams reinforced exclusively with steel bars exhibited the lowest concrete strain values in both the compressive and tensile zones, which can be attributed to the higher elastic modulus and more effective load-carrying capacity of steel reinforcement.

Figure 8 illustrates the concrete strains in the compressive and tensile zones of the Series 3 beams. This series was characterized by an identical reinforcement ratio, in which an increase in the proportion of BFRP reinforcement relative to steel led to a corresponding increase in concrete strains. The tensile strains were approximately twice those observed in the compressive zone, which is consistent with the typical flexural behavior of reinforced concrete members.

As the beams approached failure, the concrete strain values for all specimens tended to converge, indicating a similar deformation mechanism at the ultimate limit state. Prior to the formation of initial cracks, that is, up to a load level of $0.2M_u$, the relative concrete strains in both the tensile and compressive zones increased according to nearly identical patterns.

Overall, the results demonstrate that an increase in the amount of FRP reinforcement has a significant effect on concrete strain development, particularly in the tensile zone, thereby influencing the deformation behavior and serviceability performance of the reinforced concrete beams.

4 CONCLUSIONS

This study developed a standardized digital finite element workflow for comparative analysis of nine steel and hybrid steel-BFRP reinforced concrete beam configurations. ANSYS Workbench was used to maintain common geometry, loading, boundary conditions, mesh resolution, and nonlinear concrete parameters while varying longitudinal reinforcement composition.

The resulting numerical dataset enabled direct comparison of tensile and compressive concrete strain development across three reinforcement series. At the initial loading stage, the configurations exhibited similar strain evolution. After cracking, reinforcement composition increasingly affected strain redistribution. Configurations with lower longitudinal reinforcement area developed larger concrete strains, while increasing the BFRP proportion altered post-cracking tensile-strain development and the loading stage at which steel yielding occurred.

The principal contribution is the computational workflow rather than a new constitutive model. By organizing multiple beam configurations within a controlled digital model set and extracting comparable strain indicators, the approach supports repeatable configuration screening and preliminary reinforcement assessment before extensive physical testing.

The main limitation is the absence of direct experimental validation of all nine configurations. Future work should integrate numerical predictions with strain-gauge, digital image correlation, or calibrated structural-monitoring measurements. Metrological calibration and measurement uncertainty are important in digital structural monitoring [16] and should be considered when validating FEM-derived strain responses. Parameter generation and result extraction should also be automated. A digital database linking reinforcement configuration, finite element response, and design indicators would extend the workflow toward data-driven structural assessment.

REFERENCES

[1] R. Devaraj, A. Olofinjana, and C. Gerber, “Making a case for hybrid GFRP-steel reinforcement system in concrete beams: An overview,” Applied Sciences, vol. 13, p. 1463, 2023, [Online]. Available: https://doi.org/10.3390/app13031463.

[2] B. Wei, X. He, M. Zhou, H. Wang, and J. He, “Experimental study on flexural behaviors of FRP and steel bars hybrid reinforced concrete beams,” Case Studies in Construction Materials, vol. 20, p. e02759, 2024, [Online]. Available: https://doi.org/10.1016/j.cscm.2023.e02759.

[3] A. El Refai, F. Abed, and A. Al-Rahmani, “Structural performance and serviceability of concrete beams reinforced with hybrid (GFRP and steel) bars,” Construction and Building Materials, vol. 96, pp. 518-529, 2015, [Online]. Available: https://doi.org/10.1016/j.conbuildmat.2015.08.063.

[4] R. Mavlonov et al., “Analytical and experimental investigation of hybrid steel-FRP reinforced concrete beams,” Vibroengineering Procedia, vol. 60, pp. 563-570, Dec. 2025, [Online]. Available: https://doi.org/10.21595/vp.2025.25488.

[5] A. Akmaljon et al., “Tensile strength of concrete reinforced with combined steel and basalt fibers,” Vibroengineering Procedia, vol. 60, pp. 493-499, Dec. 2025, [Online]. Available: https://doi.org/10.21595/vp.2025.25372.

[6] A. Martazaev et al., “Theoretical assessment of the mechanical properties of fiber concrete using the dispersion analysis method,” Vibroengineering Procedia, vol. 60, pp. 788-794, Dec. 2025, [Online]. Available: https://doi.org/10.21595/vp.2025.25362.

[7] O. Fozilov et al., “Numerical modeling of reinforced concrete structures made of lightweight concrete using ANSYS,” Vibroengineering Procedia, vol. 60, pp. 683-689, Dec. 2025, [Online]. Available: https://doi.org/10.21595/vp.2025.25511.

[8] B. Harsono, F. M. Mahadiva, Tavio, M. M. Talipov, and H. Hermawan, “Pushover analysis of simple house structures in seismic zones,” AIP Conference Proceedings, vol. 3374, no. 1, Art. no. 050035, Mar. 2026, [Online]. Available: https://doi.org/10.1063/5.0319164.

[9] I. Mirzaev, D. Bekmirzaev, E. Kosimov, E. An, N. Nishonov, and M. Talipov, “Seismodynamics of segmented underground pipeline systems based on real earthquake records,” AIP Conference Proceedings, vol. 3447, no. 1, Art. no. 060001, May 2026, [Online]. Available: https://doi.org/10.1063/12.0044018.

[10] P. D. Nguyen, N. T. Nguyen, and V. H. Dang, “Failure mode classification for hybrid FRP/steel reinforced concrete beams: A soft computing concept based on the numerical model,” Innovative Infrastructure Solutions, vol. 9, p. 288, 2024, [Online]. Available: https://doi.org/10.1007/s41062-024-01620-4.

[11] R. Hawileh, “Finite element modeling of reinforced concrete beams with a hybrid combination of steel and aramid reinforcement,” Materials and Design, 2014, [Online]. Available: https://doi.org/10.1016/j.matdes.2014.10.004.

[12] X. Guo, Y. Dai, and J. Jiang, “Flexural behavior investigation of steel-GFRP hybrid-reinforced concrete beams based on experimental and numerical methods,” Engineering Structures, vol. 206, p. 110117, 2020, [Online]. Available: https://doi.org/10.1016/j.engstruct.2019.110117.

[13] Y. Yang, Z. Y. Sun, G. Wu, D. F. Cao, and Z. Q. Zhang, “Flexural capacity and design of hybrid FRP-steel-reinforced concrete beams,” Advances in Structural Engineering, pp. 1-15, 2019, [Online]. Available: https://doi.org/10.1177/1369433219894236.

[14] B. Zhou, R. Y. Wu, Y. Liu, X. Zhang, and S. Yin, "Flexural strength design of hybrid FRP-steel reinforced concrete beams," Materials, vol. 14, p. 6400, 2021, [Online]. Available: https://doi.org/10.3390/ma14216400.

[15] I. Zreid and M. Kaliske, "A gradient enhanced plasticity-damage microplane model for concrete," Computational Mechanics, vol. 62, no. 5, pp. 1239-1257, 2018, [Online]. Available: https://doi.org/10.1007/s00466-018-1561-1.

[16] A. Mamatov, X. Sotvoldiyev, M. Talipov, S. Shaumarov, K. Gafarbayli, and D. Bekmirzaev, "Metrological calibration and uncertainty evaluation of MEMS accelerometers for structural health monitoring in seismic regions," Vibroengineering Procedia, vol. 62, pp. 140-144, Jun. 2026, [Online]. Available: https://doi.org/10.21595/vp.2026.26360.